CHAPTER 5

ADSORPTIVE REMOVAL STUDY OF PHOSPHATE FROM WASTEWATER USING MAGNESIUM DOPED NFC/BN COMPOSITE

5.1 Introduction

The utilization of pristine NFC directly for phosphate adsorption poses challenges: (i) although cellulose is water-insoluble, it has low affinity for anions due to the predominance of neutral hydroxyl (-OH) groups; and (ii) its dense, non-porous structure impedes ion diffusion, resulting in slow adsorption kinetics [229,230]. To overcome these limitations, the development of NFC-based composite materials has gained attention. Incorporating natural clay minerals such as bentonite into NFC matrices enhances the composite's surface area, porosity, mechanical strength, and surface charge, thereby improving its performance in phosphate removal [231]. Additionally, inorganic–organic hybrid composites often show superior adsorption capabilities compared to their individual components due to synergistic effects [232,233]. Bentonite, a naturally occurring porous mineral from the smectite group, primarily composed of montmorillonite, features a 2:1 layered structure comprising two tetrahedral Si^{4+} sheets surrounding a central Al^{3+} octahedral sheet [234]. Isomorphic substitutions within this structure, such as the replacement of Si^{4+} with Al^{3+} or Al^{3+} with Mg^{2+}, confer a negative surface charge that supports ion exchange, enabling the intercalation of inorganic anions or organic polycations [235]. Owing to its high cation exchange capacity, large surface area, natural abundance, and non-toxic nature, bentonite, both in its natural and modified forms, has been extensively studied for contaminant removal, including phosphates [236,237]. The properties of BN are as follows:

Table 5.1 Properties of bentonite [231,237].

Properties	Typical Range
Chemical Composition	Mainly montmorillonite $(Na,Ca)_{0.33}(Al,Mg)_2Si_4O_{10}(OH)_2 \cdot nH_2O$; oxides: SiO_2 45–65%, Al_2O_3 9–25%, Fe_2O_3 up to 12%
Density (True/Specific)	~2.0–2.7 g/cm^3
Colour	Light grey/beige
CEC (Cation Exchange Capacity)	Typical: ~70–100 meq/100 g; MX-80 ~105 meq/100 g; Na-montmorillonite up to ~108 meq/100 g
Specific Surface Area	Basal ~740 m²/g; BET ~31.5 m²/g; Activated up to ~563 m²/g
pH (in suspension)	Slightly alkaline: ~8–10
Swelling Capacity	Can increase volume up to ~8× when hydrated; Na-bentonite swells more than Ca-bentonite

Despite the enhanced performance of advanced composite adsorbents, challenges still persist. These include electrostatic limitations stemming from the negatively charged surfaces of both NFC and bentonite, and the tendency of nano- and micro-sized adsorbents to aggregate in aqueous media, which reduces adsorption efficiency. To address these issues, we further modified the NFC/BN composite through magnesium doping, for several key reasons: (i) magnesium ions form strong complexes with phosphate, enhancing adsorption through divalent cation interactions [234]; (ii) magnesium doping promotes exfoliation of bentonite layers by intercalating NFC, increasing basal spacing and surface area for interactions; (iii) the hydroxyl-rich structures of NFC and bentonite facilitate uniform Mg distribution across the composite matrix, increasing active site exposure and improving functional performance [238];

and (iv) Mg salts are inexpensive, adding cost-effectiveness to the overall treatment process [239].

Post-adsorption handling of spent materials is another critical consideration. While many studies propose reusing phosphate-loaded adsorbents as slow-release fertilizers, they often overlook the materials' effects on soil water retention which is a key factor in sustainable agriculture, particularly in arid and semi-arid regions. Enhancing the water retention properties of adsorbents can provide dual benefits: nutrient recycling and improved water availability. Bentonite, when used as a substrate in NFC-based composites, contributes to swelling ability, thermal stability, and improved moisture retention [240]. However, the potential of Mg-doped NFC/BN composites to enhance soil water retention has not been previously reported and constitutes a novel aspect of our study.

Furthermore, the phosphate adsorption performance and mechanisms of Mg-doped NFC/BN composites remain underexplored. This research addresses these gaps by developing and evaluating a novel Mg-doped NFC/BN composite for phosphate removal from wastewater, with the added potential of post-use application in agriculture. This dual-functionality approach supports the UN Sustainable Development Goals (SDG) 12; Responsible Consumption and Production, by promoting the reuse of waste biomass to create sustainable adsorbents, and SDG 14, Life Below Water, by mitigating phosphate-induced eutrophication, thereby preserving aquatic ecosystems.

5.2 Synthesis of NFC/BN composite adsorbent

NFC was extracted from sugarcane bagasse using the method reported in our previous study [211]. A series of NFC/BN composite adsorbents were prepared by mixing varying mass ratios of NFC and BN (Table 5.2) in a beaker containing 100 mL of distilled water for 12 h. It was then filtered and dried at 80 °C for further use. The composites were designated with subscripts corresponding to their mass ratios.

Next, the NFC/BN composite (that exhibited highest removal efficiency), was combined with 100 mL of 1.5 M $MgCl_2 \cdot 6H_2O$ in a beaker. The prepared mixture was ultrasonicated for approximately 15 min at ambient temperature to obtain better dispersion and homogeneity. Thereafter, 0.1 M NaOH solution was gradually added to the mixture until the pH reached 10 while vigorously stirring at room temperature for a duration of 6 h. The purpose of alkali treatment in the aforementioned step was to coat magnesium ions onto the NFC/BN composite surface. Following this, the mixture was aged at room temperature for 24 h, filtered and washed repeatedly with distilled water to eliminate any traces of chloride ions. The fractions were dried overnight at 80 ºC, gently ground, and passed through a 0.15 mm mesh to obtain a fine powder consistency. Figure 5.1 illustrates the schematic representation of adsorbent synthesized using NFC, BN and $MgCl_2$. The obtained composite was labelled as Mg@NFC/BN for understanding.

Table 5.2 Composition of adsorbents prepared with different mass ratios of NFC, BN, and $MgCl_2$.

Adsorbents	NFC:BN (mass ratios)	$MgCl_2$
NFC_1/BN_1	1:1	0
NFC_2/BN_1	2:1	0
NFC_4/BN_1	4:1	0
NFC_1/BN_2	1:2	0

NFC_1/BN_4	1:4	0
$Mg@NFC_1/BN_1$	1:1	1.5 M

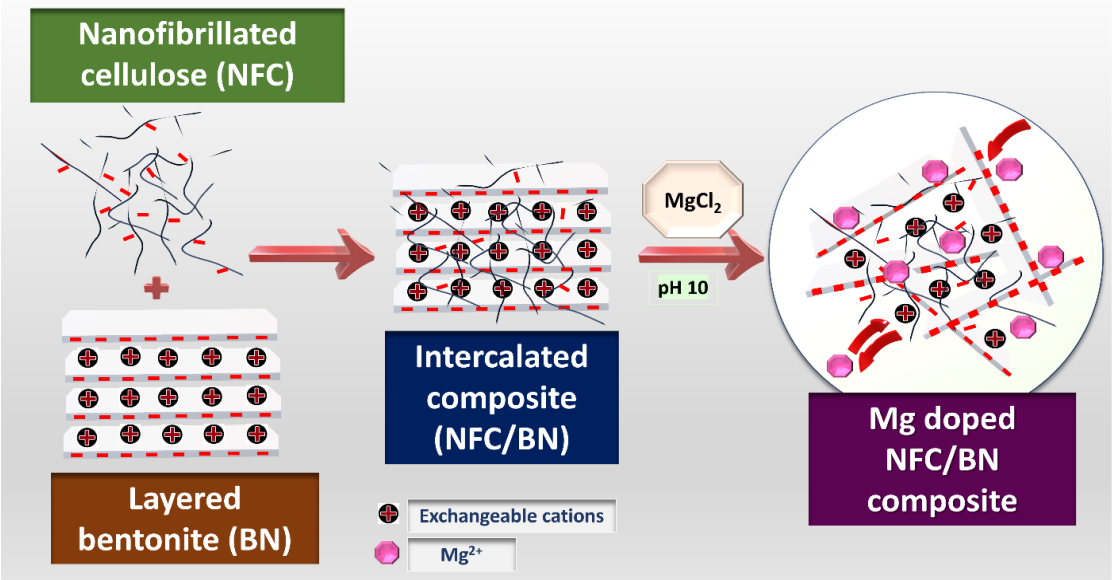

Figure 5.1 Schematic diagram depicting the fabrication process of Mg doped NFC/BN.

5.3 Results and discussions

5.3.1 Characterization of synthesized adsorbent

5.3.1.1 Scanning Electron Microscopy and Energy Dispersive Spectroscopy (SEM-EDS)

The surface morphology and elemental composition of the NFC/BN composite, as well as Mg@NFC/BN samples before and after phosphate sorption, were examined using Field Emission Scanning Electron Microscopy (FESEM) in tandem with Energy Dispersive X-ray Spectroscopy (EDS), with the results illustrated in Figure 5.2. The FESEM micrograph of the NFC/BN composite reveals a disrupted three-dimensional burr-like morphology, where NFC functions as a reinforcing agent within the bentonite clay matrix (Figure 5.2 a). The absence of a distinct fibrous NFC structure in the images

suggests its successful intercalation within the interlayer spaces of bentonite, likely facilitated by hydrogen bonding [241]. This structural integration enhances the composite's stability and dispersion characteristics, contributing to its improved performance in phosphate removal. The subsequent incorporation of magnesium into the NFC/BN composite induces exfoliation of the structure, leading to the formation of more layered and elongated fragments, thereby increasing the exposed surface area. Additionally, distinct metal sediments were observed to be adhered across the composite surface, contributing to an increase in active sites for adsorption (Figure 5.2 b). Following phosphate adsorption, the surface morphology of Mg@NFC/BN undergoes further modification, with the appearance of cloud-like deposits on the surface, indicating the successful adsorption of phosphate ions onto the composite (Figure 5.2 c). Figure 5.2 d shows the high-resolution surface architecture of the adsorbent after phosphate adsorption.

The EDS element content of adsorbent before and after adsorption are shown in Figure 5.2 e and f. The surface of Mg@NFC/BN mainly contained constituent elements such as C, O, Al and Si of NFC and bentonite well distributed on the synthesized composite surface. The detected presence of Mg (15.26 %), confirms successful integration of Mg in NFC/BN composite which is in agreement with FTIR result. Furthermore, the post-adsorption samples exhibit the presence of P, indicating effective phosphate uptake. This validates the composite's enhanced adsorption efficiency, attributed to its structural characteristics and improved metal interaction sites [134]. The elemental composition, expressed in weight percentages, is further substantiated by EDX elemental mapping analysis images of phosphate loaded Mg@NFC/BN (Figure 5.2 g).

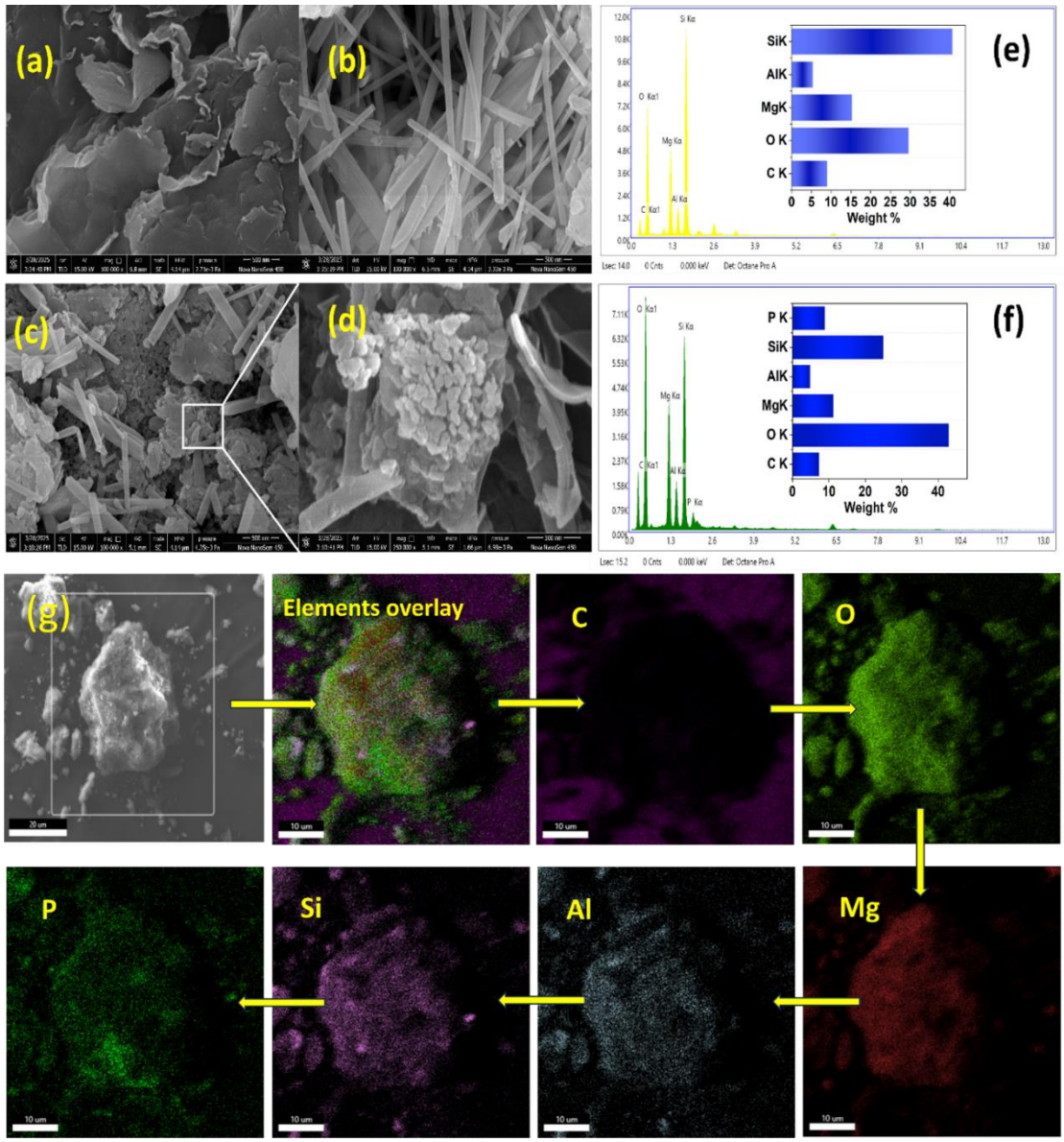

Figure 5.2 SEM images of; (a) NFC/BN; (b & c) Mg@NFC/BN (pre and post phosphate adsorption respectively); (d) high resolution SEM micrograph of Mg@NFC/BN (post adsorption); (e & f) EDS spectra and corresponding element distribution content of Mg@NFC/BN (pre and post phosphate adsorption respectively) (g) EDS elemental mapping of C, O, Mg, Al, Si, and P of Mg@NFC/BN (after adsorption).

5.3.1.2 Fourier Transform Infrared Spectroscopy (FT-IR)

The formation of the hybrid composite was verified through FT-IR analysis, which involved comparing the surface modifications of functional group on NFC, BN, NFC/BN composite, and Mg@NFC/BN (pre and post adsorption) (Figure 5.3 a). For NFC, derived from natural cellulose, the FT-IR spectrum displayed distinct absorption bands indicative of its functional groups. The broad band observed around 3400 cm^{-1} region corresponds to the stretching vibrations of O-H bonds including those associated with hydroxyl functional groups, intermolecular hydrogen bonding, and free or bound water molecules. The distinctive peaks of cellulose are observed at approximately 2914 cm^{-1} and 1375 cm^{-1} (C-H bending), and 1140 cm^{-1} (C-O-C pyranose ring) [242]. Additionally, the peaks at 1049 cm^{-1} and 893 cm^{-1} are associated with C–O stretching and glycosidic ether bond of β-1,4-glycosidic ring linkages between the D-glucose units in cellulose, respectively [211]. The FT-IR analysis of the raw bentonite clay sample, primarily composed of montmorillonite, confirmed the presence of structural Si–OH and Al–OH groups, along with intercalated water layers, as evidenced by peaks at 3410 cm^{-1} and 1635 cm^{-1} [243]. The strong band at 1035 cm^{-1} correspond to Si-O bond vibrations in montmorillonite, while Al-O vibrational peak appeared at 820 cm^{-1} [244]. The vibrational peak at 912 cm^{-1} corresponds to the -OH bending associated with $Al(OH)_3$ in the bentonite structure. The peaks at 730 cm^{-1}, and 464 cm^{-1} correspond to Si-O-Si vibrations, while the peaks at 664 cm^{-1} and 500 cm^{-1} are associated with the bending vibrations of octahedral Al-O-Si of bentonite [245].

The FT-IR spectrum of the synthesized NFC/BN composite exhibited a complex profile, demonstrating that all characteristic peaks of both NFC and BN were preserved; confirming incorporation of NFC with BN. The bands particularly in the O–H stretching region (~3400 cm^{-1}) broadened maybe due to formation of hydrogen

bonding between NFC and BN. Furthermore, the prominent bands corresponding to the integrated cellulose (e.g., O–H, C–H, and C–O stretching vibrations) and bentonite (Si–O and Al–O vibrations) were observed at slightly shifted positions and intensity change, suggesting strong interactions between the two components.

The FT-IR spectra of Mg-doped NFC/BN revealed a prominent peak at 3690 cm^{-1}, corresponding to the –OH stretching vibration in $Mg(OH)_2$, alongside a peak at 546 cm^{-1}, attributed to the Mg–O stretching vibration, confirming the successful incorporation of Mg into the composite [246]. The characteristic C–H stretching band of cellulose (~2914 cm^{-1}) displayed a reduction in intensity, likely due to structural modifications or interactions between Mg^{2+} and functional groups within the composite. Notably, the absorption peaks at 3410 cm^{-1} and 1635 cm^{-1} significantly weakened, suggesting that H^+ ions in surface hydroxyl groups (Al–OH and Si–OH) underwent an ion-exchange reaction with Mg^{2+} ions. Furthermore, the faint peaks observed at 833 cm^{-1} and 458 cm^{-1} were attributed to deformation vibrational modes of Al–O–Mg and Si–O–Mg bonds, indicating the presence of cation exchangeable Mg^{2+} onto the composite matrix, which is in agreement with EDS analysis [247]. In the post-adsorption samples, significant deviations were observed, likely modifying the vibrational modes of existing functional groups and resulting in altered and relocated bands. Symmetric and asymmetric stretching vibrations within the 1000–1100 cm^{-1} range, attributed to phosphorus (P=O) functional group of phosphate ions, were clearly evident. Concurrently, the band at approximately 546 cm^{-1}, associated with Mg–O, nearly disappears. These findings provide clear evidence of adsorption of phosphate onto the synthesized adsorbent.

5.3.1.3 X-ray Diffraction (XRD)

The XRD profiles of pristine NFC, BN, NFC/BN, and Mg@NFC/BN composites were analyzed to determine the phase composition, sample purity, and structural transitions (Figure 5.3 b). The diffraction pattern of raw bentonite confirmed its enrichment in montmorillonite as the predominant clay phase, with characteristic peaks observed at 6.99°, 19.86°, 20.9°, 24.9°, 26.68°, 34.88°, and 36.6° (reference no. 01-088-0891 and 00-033-1200) [248]. For NFC, peaks at 16.1°, 22.4°, and 34.5° correspond to the (110), (200), and (040) crystallographic planes of cellulose I, confirming its structural integrity [249]. The XRD pattern of the NFC/BN composite exhibited integration of primary diffraction peaks from both NFC and BN, accompanied by a decrease in peak intensity. This reduction in intensity suggests successful composite formation, where NFC is well distributed across the bentonite surface and intercalated within the clay layers. Upon Mg ion incorporation into the NFC/BN matrix, the XRD pattern of Mg@NFC/BN revealed further attenuation of peak intensities, along with the appearance of new peaks, indicative of magnesium-containing phases such as MgO, $Mg(OH)_2$, and $Mg(SiO_3)$ (reference no: 00-002-1207, 01-082-2454 and 01-082-1644) [250]. These structural modifications confirm the successful integration of Mg ions into the composite matrix. Furthermore, the XRD findings are in strong agreement with FT-IR and XPS analyses, further supporting the structural and compositional changes in Mg@NFC/BN composite.

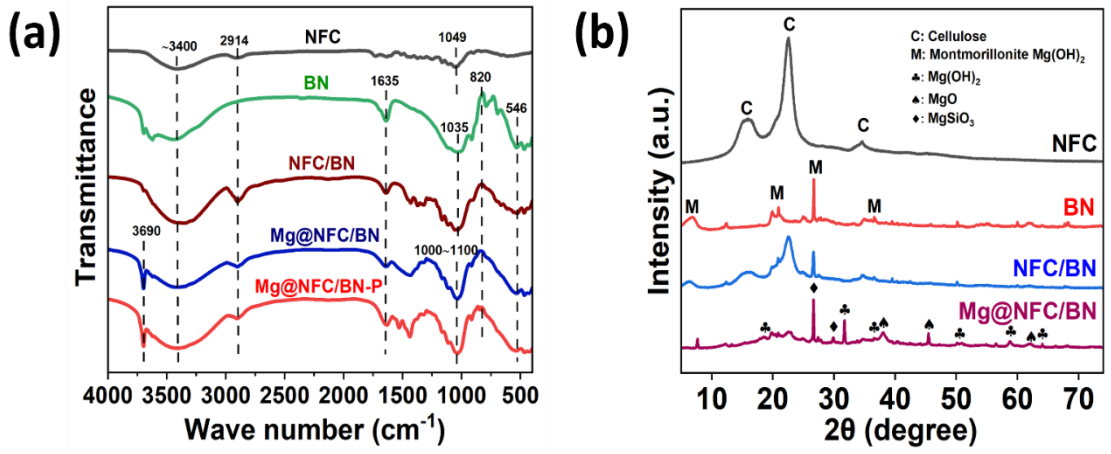

Figure 5.3 FTIR spectra of (a) NFC, BN, NFC/BN composite, Mg doped NFC/BN (before and after adsorption); (b) XRD patterns of pristine NFC, BN NFC/BN composite and Mg doped NFC/BN.

5.3.2 Preliminary assessment: Effect of different ratios of NFC and BN in phosphate removal studies

The removal efficiency of native nanofibrillated cellulose, raw BN, NFC/BN composite, and Mg@NFC/BN at varying ratios were investigated, and their adsorption capacities towards phosphate were evaluated. Figure 5.4 a show that the overall adsorption performance of NFC/BN composite and Mg doped NFC/BN composite on phosphate is better than that of pristine NFC and raw BN. The adsorption capacities of NFC, BN, NFC/BN composites, and Mg@NFC/BN showed a trend of Mg@NFC_1/BN_1 > NFC_1/BN_1 > NFC_2/BN_1 > NFC_1/BN_2 > NFC_4/BN_1 > NFC_1/BN_4 > NFC > BN. This behaviour is ascribed to the synergetic effect between nanofibrillated cellulose and bentonite clay, which promotes cooperative interactions, resulting in a higher adsorption capacity than that of either material alone. Among the NFC/BN composites, NFC_1/BN_1 depicted the highest phosphate removal efficiency of 80.1%. This is because NFC provides abundant hydroxyl groups, facilitating hydrogen bonding and electrostatic interactions with phosphate while bentonite, a layered clay, enhances

adsorption by providing additional binding sites and interlayer spaces for phosphate capture. In addition, the balanced proportion of NFC and BN optimized the surface properties and adsorption sites of the composite adsorbent, thereby improving its overall performance. Conversely, NFC_4/BN_1 and NFC_1/BN_4 exhibited lower adsorption efficiency, even in composite form. This may be attributed to the increased viscosity at higher NFC concentrations, which impedes the uniform dispersion of NFC and BN. Notably, a 4:1 NFC-to-BN ratio was not utilized for metal doping due to anticipated challenges in maintaining an even and effective distribution [251]. Similar limitation lies in nanocellulose-clay composites at higher clay loadings i.e., maintaining dispersion, as increased clay content does not necessarily corelate with improved adsorption capacity. For instance, when bentonite clay concentration was increased from 1 to 4, the phosphate adsorption capacity of NFC/BN composite decreased from 16.2 mg g^{-1} to 9.15 mg g^{-1}. This decline is likely due to clay aggregation and reduced pore accessibility at higher clay concentrations [252]. Given its excellent adsorption performance and cost-effectiveness, NFC_1/BN_1 ratio was taken into consideration for Mg. The resulting Mg-doped NFC_1/BN_1 composite exhibited the highest adsorption capacity of approximately 19.2 mg/g and removal efficiency of 88.6%. This enhancement may be resulting from metal ion modification, which increases phosphate adsorption capacity by reducing the negative charge and elevating the isoelectric point (PZC) of the NFC/BN composite [253]. Taking into account the adsorption performance, magnesium doped NFC/BN composite with optimal ratio combination was chosen for subsequent studies.

5.3.3 Batch adsorption studies

5.3.3.1 Effect of pH

The pH significantly influences the surface charge of the adsorbent as well as the removal and uptake of ions at the water-adsorbent interface (Figure 5.4 b). The speciation of orthophosphate, including H_3PO_4, $H_2PO_4^-$, HPO_4^{2-}, and PO_4^{3-}, is governed by the solution pH values of < 2.0, 2.0–7.0, 7.0–12.0 and > 12.0 respectively, based on their corresponding dissociation constants (pK_a) [254]. The adsorption free energy of $H_2PO_4^-$ was lower than that of HPO_4^{2-}, indicating that $H_2PO_4^-$ was more readily adsorbed onto the surfaces of Mg@NFC/BN composites compared to HPO_4^{2-} [255]. The effect of pH on the removal of phosphate was assayed at different pH values ranging from 2 to 11. Mg@NFC/BN demonstrated outstanding phosphate removal efficiency under acidic conditions, while an increase in solution pH led to a noticeable reduction in the adsorption performance. As shown in the figure, a consistent and effective removal was observed within the pH range of 4 to 7, where H_2PO4^- was the dominant species, facilitating strong binding with Mg^{2+} and resulting in high adsorption efficiency. However, at pH levels above 7, a gradual decline in adsorption capacity was evident. The figure indicates that the highest removal percentage and adsorption capacity within pH 4 to 9 varied between 93.8 to 78.57 % and 20.01 to 14.89 mg/g, respectively. This trend can be attributed to the influence of the adsorbent's surface charge. As observed in Figure 5.4 c, the point of zero charge (PZC) of Mg@NFC/BN was identified at approximately 8.9. This suggests that when the pH is below 8.9, the surface of the adsorbent becomes protonated, procuring a positive charge that enhances electrostatic attraction with anionic phosphate species in the solution. In contrast, when the pH exceeds 8.9, the surface charge shifts to negative, leading to electrostatic repulsion of anions and a subsequent decline in phosphate adsorption capacity. Post sorption, the PZC of the adsorbent shifted to 7.6, indicating a pronounced reduction

from its initial value. This decrease was attributed to surface charge neutralization resulting from site protonation occurring near the metal-loaded surface within the shear plane [256]. At pH ≥ 3, the adsorbent exhibited relatively lower removal efficiency and adsorption capacity, approximately 23.7% and 5.14 mg/g, respectively. This reduction is associated to phosphate speciation, where H_3PO_4 predominates, making adsorption less favourable. Alternatively, when the pH surpasses 9.0, a sharp decline in adsorption capacity is observed [257]. This is likely due to the high concentration of hydroxide ions competing with phosphate for active adsorption sites, coupled with increased electrostatic repulsion in the highly alkaline medium. Furthermore, the decrease in phosphate removal at elevated pH levels is also associated with a shift in phosphate speciation from $H_2PO_4^-$ and HPO_4^{2-}, in concurrence with a reduction in protonation rates.

Additionally, when the initial pH ranged between 3 and 6, the equilibrium pH of the solution elevated to around 9.0. This increase in pH was mainly due to a ligand exchange reaction, in which $H_2PO_4^-$ replaced –OH groups on the composite surface, leading to inner sphere complexation and the release of OH^- into the solution [258]. The findings indicated that Mg@NFC/BN is a sustainable option for phosphate removal in conventional wastewater treatment, as the pH of wastewater typically ranges from 5.0 to 8.0.

5.3.3.2 Effect of adsorbent dose

The effect of adsorbent dosage on phosphate removal was investigated to determine the optimal dosage for maximum removal efficiency while maintaining constant volume and initial phosphate concentration (Figure 5.4 d). The results indicate that optimizing

this parameter can significantly reduce the required adsorbent amount while achieving high removal efficiency. As the dosage of Mg@NFC/BN increased from 0.5 to 2.5 g/L, the phosphate removal efficiency improved markedly from 42.7% to 91.4%. However, the phosphate adsorption capacity exhibited a decreasing trend with increasing adsorbent dosage. This decline could be attributed to the agglomeration of excess adsorbent, that limits the effective utilization of adsorption sites, thereby reducing the adsorption capacity [259]. Notably, an adsorbent dosage of 1 g/L exhibited a removal efficiency of 88.5%, which corresponded well with a favourable adsorption capacity of 19.17 mg/g. Therefore, taking into account both economic feasibility and removal performance, 1 g/L was deemed as the optimal dosage.

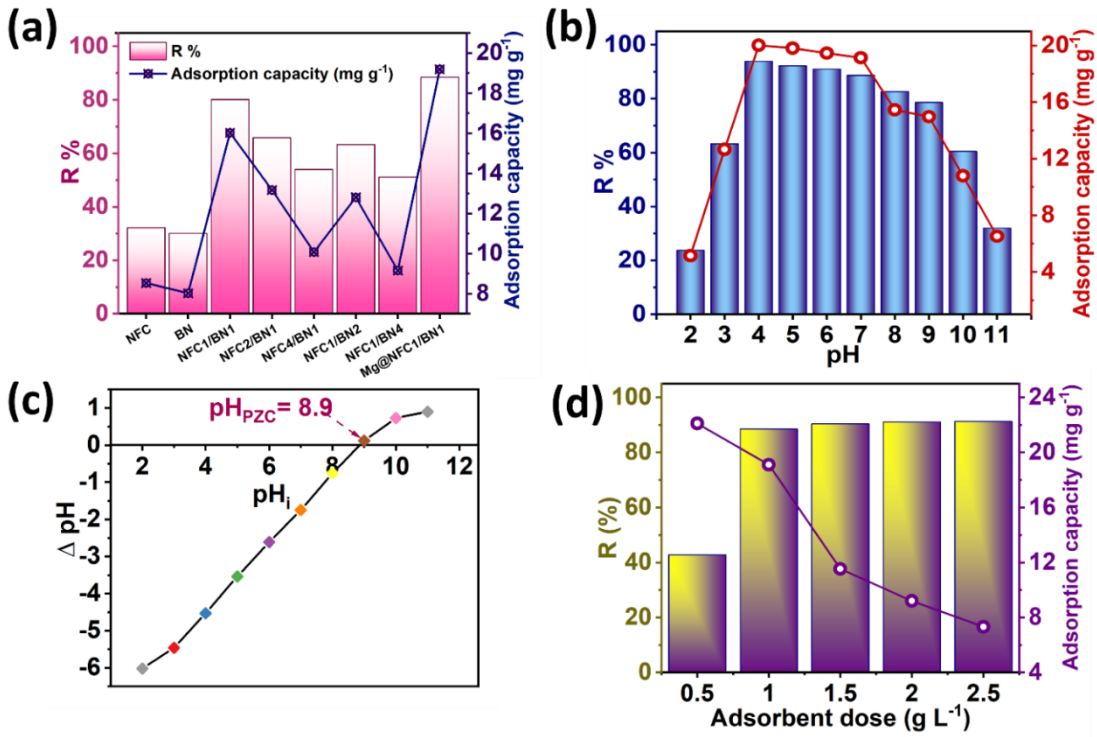

Figure 5.4 (a) Pre-screen adsorption of pristine NFC, BN, NFC/BN composites (with varying molar ratios) and Mg doped NFC/BN; (b) effect of different pH values (2-11) on phosphate removal (initial conc. 20 mg/L, dose 1 g/L, contact time 90 min); (c) pH_{PZC} value of Mg@NFC/BN and; (d) effect of adsorbent dose (0.5-2.5 g/L) on phosphate removal by Mg@NFC/BN (initial conc. 20 mg/L, initial pH 7.0 ± 0.2, contact time 90 min).

5.3.3.3 Adsorption kinetic studies

The experimental data were modelled by Pseudo-first-order (PFO) and Pseudo-second-order (PSO) models (Figure 5.5 a). As evident from the figure, the phosphate adsorption onto Mg@NFC/BN proceeded rapidly during the initial 30 min, followed by a slower phase until equilibrium was reached at approximately 90 min. This trend can be attributed to the progressive saturation of available adsorption sites. According to the kinetic parameters summarized in Table 5.3, both the pseudo-first-order and pseudo-second-order models yielded high correlation coefficients ($R^2 > 0.9$), indicating good agreement with the experimental data. However, a closer comparison of the R^2 values reveals that the pseudo-second-order model provided a better fit, with a higher R^2 value when considering the second decimal place. Furthermore, the calculated adsorption capacity ($q_{e\ cal}$) derived from the pseudo-second-order model closely matched the experimental data (q_{exp}), confirming that the adsorption of phosphate onto Mg@NFC/BN is predominantly governed by chemisorption mechanism [260].

Table 5.3 Kinetic parameters of the phosphate removal onto Mg@NFC/BN.

Models	Parameters	Mg@NFC/BN
Pseudo-first-order kinetic model	$q_{e\ cal}$ (mg/g)	23.27
	k_1 (min^{-1})	0.04
	R^2	0.98
Pseudo-second-order kinetic model	$q_{e\ cal}$	19.33
	k_2 ($g/mg/min^{-1}$)	0.0022
	R^2	**0.99**

5.3.3.4 Adsorption isotherm studies

To gain deeper insight into the solid–liquid adsorption behaviour, both Langmuir and Freundlich isotherm models were applied to describe the equilibrium data. The adsorption isotherm data for phosphate on Mg@NFC/BN at varying initial concentrations and different temperatures (298.5 K, 308.5 K, and 318.5 K) is presented in Figure 5.5 b. As shown, the adsorption capacity (q_{max}) increased with increasing initial phosphate concentrations, which can be attributed to the enhanced mass transfer driving force at higher concentrations [261]. At an initial phosphate concentration of 20 mg/L and temperature of 298.5 K, the adsorption capacity reached 19.2 mg/g. Moreover, the gradual decline in the maximum adsorption capacity (Q_0), as estimated from the Langmuir isotherm model with increasing temperature, suggesting that the adsorption process is likely exothermic in nature. The corresponding isotherm constants and regression coefficients with respect to different temperatures are summarized in Table 5.4. Notably, the Langmuir model exhibited higher correlation coefficients ($R^2 \geq 0.9644$) compared to the Freundlich model ($R^2 \geq 0.8887$), indicating a better fit to the experimental data. These results imply that phosphate adsorption onto Mg@NFC/BN occurs predominantly via monolayer adsorption on a homogeneous surface [262].

Table 5.4 Isotherm parameters of the phosphate removal onto Mg@NFC/BN at different temperatures (298.5 K, 308.5 K and 318.5 K).

Models	T (K)	Parameters	Mg@NFC/BN
Langmuir isotherm model	**298.5**	Q_0 (mg/g)	44.7
		K_L (L/mg)	0.27
		R^2	**0.99**
	308.5	Q_0 (mg/g)	38.45
		K_L (L/mg)	0.16
		R^2	0.96
	318.5	Q_0 (mg/g)	32.05
		K_L (L/mg)	0.107

		R^2	0.97
Freundlich isotherm model	**298.5**	K_F $(mg/g)(L/mg)^{(1/n)}$	12.67
		n_F	3.14
		R^2	0.88
	308.5	K_F $(mg/g)(L/mg)^{(1/n)}$	9.67
		n_F	3.02
		R^2	0.92
	318.5	K_F $(mg/g)(L/mg)^{(1/n)}$	6.05
		n_F	2.73
		R^2	0.89

5.3.3.5 Effect of co-existing anions on phosphate removal

Wastewater from industrial processes, mining and metal processing typically contains other co-existing anions such as Cl^-, SO_4^{2-}, and CO_3^{2-} (HCO_3^-) along with PO_4^{3-}. During the production processes in certain industrial parks, the wastewater generated contains lithium hexafluorophosphate ($LiPF_6$) that contains a significant amount of fluoride (F^-) and phosphate ions [263]. Additionally, nitrogen and phosphorus are common pollutants in wastewater originated from domestic sewage, agricultural runoff, industrial effluents, aquaculture waste, and landfill leachate. These anions can impact the phosphate removal efficiency of adsorbents. Hence, to evaluate the adsorption behaviour of Mg@NFC/BN for phosphate in complex solutions i.e., the presence of various interfering anions, we performed competitive adsorption experiments using different anion concentrations (1 mM/L, 10 mM/L, and 100 mM/L). Figure 5.5 c illustrates the phosphate removal efficiency of the synthesized adsorbent, and it can be

seen that at lower concentrations of all coexisting ions, the removal efficiency remains largely unaffected. In contrast, as the concentration of these ions increases, their impact on the removal efficiency is only slightly affected. The results reveal that phosphate removal efficiency of Mg@NFC/BN is minimally affected in the presence of Cl^- (2.33 %), NO_3^- (1.27 %), and F^- (5.41 %) ions, despite an increase in their concentration from 1 to 100 mM/L. The inhibitory effect of these anions on phosphate adsorption follows the order; $F^- > Cl^- > NO_3^-$. This can be attributed to the fact that competition from other anions is influenced by their charge density and ionic radii. The ionic radii of $H_2PO_4^-$ (~ 0.24 nm) is relatively larger and has higher charge density than Cl^- (0.18 nm), NO_3^- (0.179 nm), and F^- (0.13 nm). This suggests that among these anions, fluoride exhibits the strongest competition due to its small size and high charge density, chloride shows moderate competition but is less effective than F^- while NO_3^-, due to its large size and delocalized charge, has the weakest competition and least inhibitory effect [264]. The inhibition effect of SO_4^{2-} (100 mM/L) led to a notable decrease in the phosphate removal efficiency of Mg@NFC/BN. This can be ascribed to the ionic radii of SO_4^{2-} ions (0.23 nm) which is comparable to the ionic radii of phosphate [223]. Despite lower charge density, it strongly interacts with positively charged adsorption sites, leading to competitive adsorption. However, phosphate forms inner-sphere complexes through strong covalent bonding while sulphate typically forms outer-sphere complexes through weak electrostatic interactions, but at high concentrations, it can still disrupt phosphate adsorption by blocking active sites. However, the phosphate removal efficiency could only decrease by 19.2 % at concentration of 100 mM/L. Among various anions, HCO^{3-} exhibited the most significant impact, reducing phosphate removal efficiency by 18.24 %, 26.3 % and 29.68 % at concentrations of 1,

10, and 100 mM/L, respectively, compared to the control group. As the concentration of HCO_3^- increased, phosphate removal efficiency further declined. The presence of HCO^{3-} could elevate the solution's pH, which was not favourable to phosphate adsorption. However, high concentrations of HCO^{3-} were seldom encountered in actual wastewater, enabling Mg@NFC/BN to effectively adsorb phosphate through inner-sphere complexation [260].

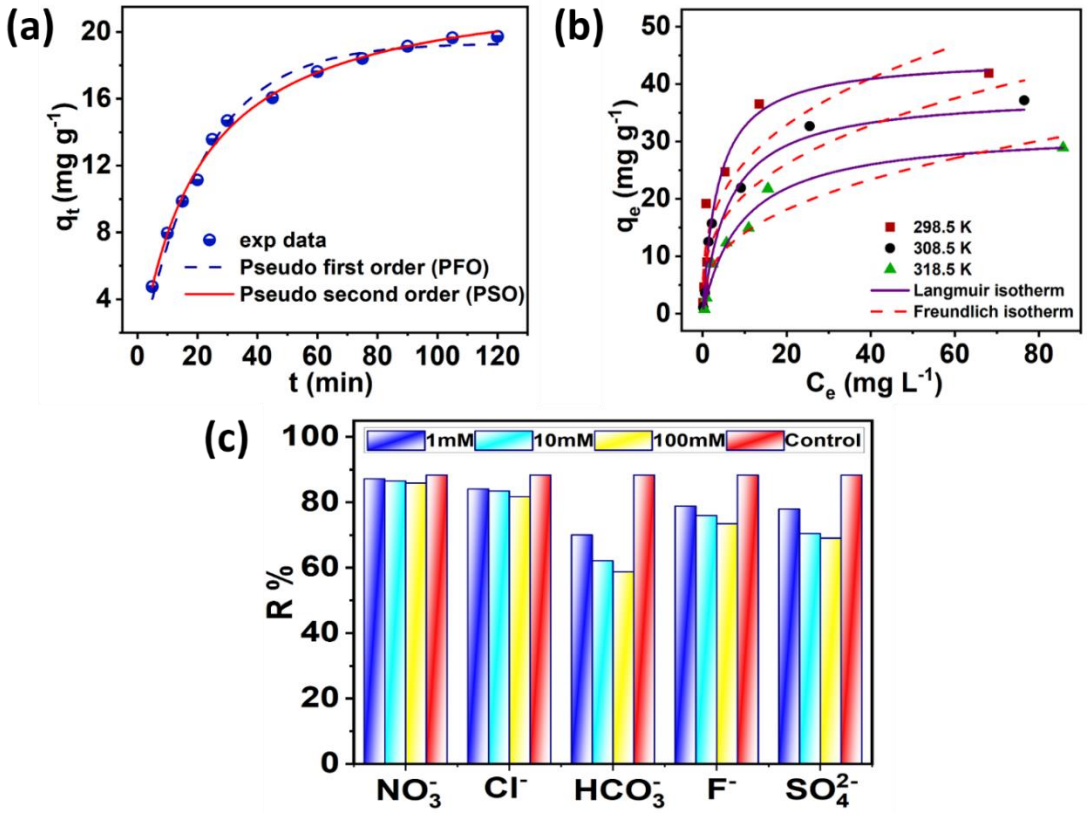

Figure 5.5 (a) Effect of different contact time (0-120 min) on phosphate removal by Mg@NFC/BN and adsorption kinetics (initial conc. 20 mg/L, dose 1 g/L, initial pH 7.0 ± 0.2); (b) Effect of different initial concentration (2, 5, 10, 20, 30, 50 and 100 mg/L) on phosphate removal by Mg@NFC/BN and adsorption isotherm (at varying temperature (298.5K, 308.5 K and 318.5 K), adsorbent dose 1 g/L, initial pH 7.0 ± 0.2, contact time 90 min); the points and lines depict the experimental data and fitting curves of kinetic and isotherm models, respectively; (c) effect of co-existing anions typically found at different values in wastewaters (1, 10 100 mM concentration).

5.3.3.6 Adsorption thermodynamic studies

The spontaneity and thermodynamic behaviour of phosphate adsorption onto Mg@NFC/BN were evaluated based on thermodynamic parameters, including changes in standard Gibbs free energy (ΔG^0), enthalpy (ΔH^0), and entropy (ΔS^0), calculated using the equations provided in the Chapter 2. The linear plot of $\ln(q_e/C_e)$ versus $1/T$ (Figure 5.6 a) and the corresponding thermodynamic data are provided in Table 5.5. The negative values of ΔG^0 at all studied temperatures confirm that phosphate adsorption is both feasible and spontaneous under experimental conditions [265]. Furthermore, increasing ΔG^0 values shifting from −7.84 kJ/mol at 298.5 K to −2.109 kJ/mol at 318.5 K, indicating that the adsorption process is more favourable at lower temperatures, with a gradual decline in spontaneity as temperature rises [266]. The ΔH^0 value of −93.37 kJ/mol suggests an exothermic adsorption process, that is consistent with isothermal studies, demonstrated a decrease in adsorption capacity with increasing temperature. Additionally, the negative ΔS^0 indicates a decrease in interface randomness between Mg@NFC/BN and aqueous solution during adsorption process, possibly due to strong interactions such as chemisorption, which is in line with observations from kinetic studies.

Table 5.5 Thermodynamic parameters of the phosphate removal onto Mg@NFC/BN at different temperatures (298.5 K, 308.5 K and 318.5 K).

T (K)	K_d	ΔG^0 (kJ mol^{-1})	ΔH^0 (kJ mol^{-1})	ΔS^0 (kJ mol^{-1} K)
298.5	23.2	-7.84	-93.37	-2.87
308.5	7.16	-4.97		
318.5	2.18	-2.11		

5.4 Water retention capacity of soil with PLC

Water retention refers to the ability to store and retain water in soil, which helps mitigate the effects of extreme climatic events and reduces the risk of flooding [267]. To

evaluate this, the water-retention capacity of soil was examined under varying PLC application rates (Figure 5.6 b). Results demonstrated that incorporating PLC significantly improved the soil's ability to retain water. After 30 days of incubation, soils treated with 0.5 %, 1 %, and 2 % PLC exhibited 3.86 %, 7.03 %, and 14.34 % higher water retention, respectively, compared to the control group (without PLC). In the control group, water retention rapidly dropped to around 50 % by the 6th day. However, in soils amended with PLC, this threshold was reached on the 7th, 11th, and 14th day, depending on the PLC application rate of 0.5%, 1% and 2% respectively. By the 25th day, the control soil had nearly lost all retained moisture, whereas the soil samples with 0.5 %, 1 %, and 2 % PLC still maintained 7.31 %, 12.99 %, and 20.34 % water content, respectively. This enhancement is largely attributed to the hydrophilic properties cellulosic materials, along with the increased porosity resulting from the integration of bentonite into the cellulosic structure [268]. Overall, these results indicate that using PLC can substantially boost the soil's ability to retain water, thereby contributing to effective water conservation, especially in arid and semi-arid regions.

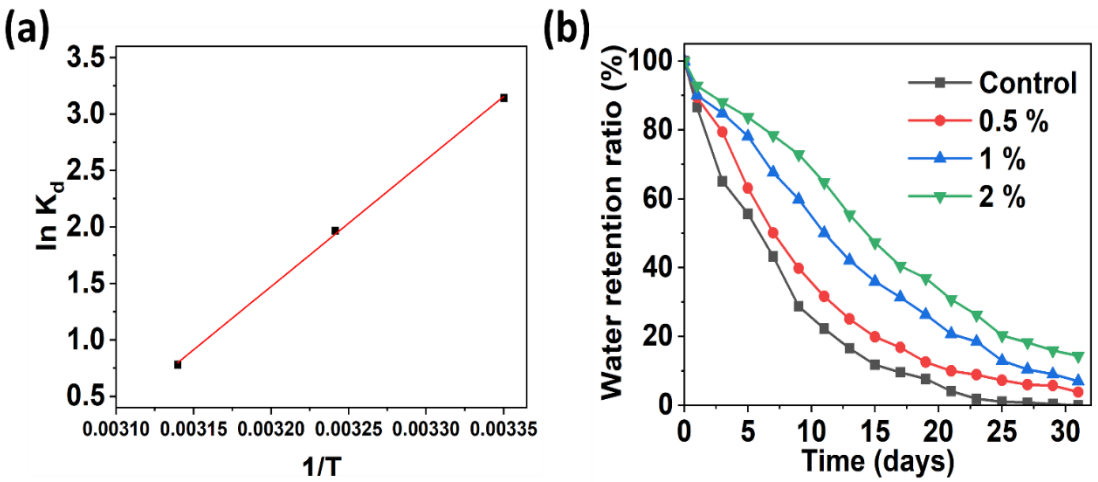

Figure 5.6 (a) Linear plot of ln(qe/Ce) versus 1/T; (b) Water-retention property of soil samples: (■) control (without PLC), (●) 0.5 % PLC, (▲) 1% PLC and (▼) 2% PLC.

5.5 XPS studies and proposed adsorption mechanism of phosphate removal

X-ray Photoelectron Spectroscopy (XPS) patterns of Mg@NFC/BN samples before and after adsorption were compared to analyze the chemical states of elements involved in phosphate removal and gain detailed insights into the interaction mechanism at the solid/water interface (Figure 5.7). As anticipated, the result of survey scan exhibited all the characteristic peaks of elements involved and successful Mg engineering on NFC/BN surface (Figure 5.7 a). Furthermore, the emergence of P 2p peak in the XPS spectra after adsorption clearly validates the uptake of phosphate onto the surface. As illustrated in high resolution XPS spectra of P 2p (Figure 5.7 b), it showed a characteristic doublet, which can be deconvoluted into two distinct peaks, corresponding to P–O ($2P_{1/2}$) and P=O ($2P_{3/2}$) positioned at 132.8 eV and 133.7 eV [269]. The observed doublet separation $P_{3/2}$–$P_{1/2}$ equals 0.89 eV, which indicate presence of phosphate groups (PO_4^{3-} and HPO_4^{2-}) respectively, indicating successful adsorption of phosphate ions over the adsorbent's surface [270,271].

As shown in Figure 5.7 c, the high-resolution O 1s spectrum of Mg@NFC/BN before adsorption was deconvoluted into three distinct peaks at 530.8 eV, 531.77 eV, and 535.83 eV. These peaks correspond to lattice oxygen (O_L), hydroxyl oxygen (O_H), and physisorbed water, respectively, based on the binding energies of different oxygen species [256,272]. The O_L and O_H components represent metal–oxygen (M–O) and metal–hydroxyl (M–OH) bonds, respectively. After adsorption (Figure 5.7 d), a significant decrease in the proportion of M–O and M–OH peaks were observed, along with the disappearance of the physisorbed water peak at 536 eV. This can be attributed to ligand exchange, where –OH groups and physisorbed water molecules are replaced, leading to the formation of stable M–O–P (Mg) inner-sphere complexes during the

adsorption process. In the Mg 1 s spectra (Figure 5.7 e and f), the deconvoluted peaks at 1304 eV and 1303.01 eV corresponding to Mg-O and Mg-OH shifted to 1303.42 eV and 1302.7 eV post adsorption, respectively [273]. This change in the binding energies of Mg 1s indicates formation of $Mg_3(PO_4)_2$ and $MgHPO_4$ aligning with the data obtained from O 1s XPS peaks. The protonated MgO in the solution facilitates phosphate anion capture through inner-sphere complexation, driven by ligand exchange between phosphate and hydroxyl groups [269]. While the Mg 1s peak fitting suggests the formation of $Mg_3(PO_4)_2$ and $MgHPO_4$ species, the possible coexistence of unreacted MgO and $Mg(OH)_2$ cannot be completely excluded due to spectral overlap; thus, the deconvolution represents an approximate interpretation supported by corresponding O 1s and P 2p spectra.

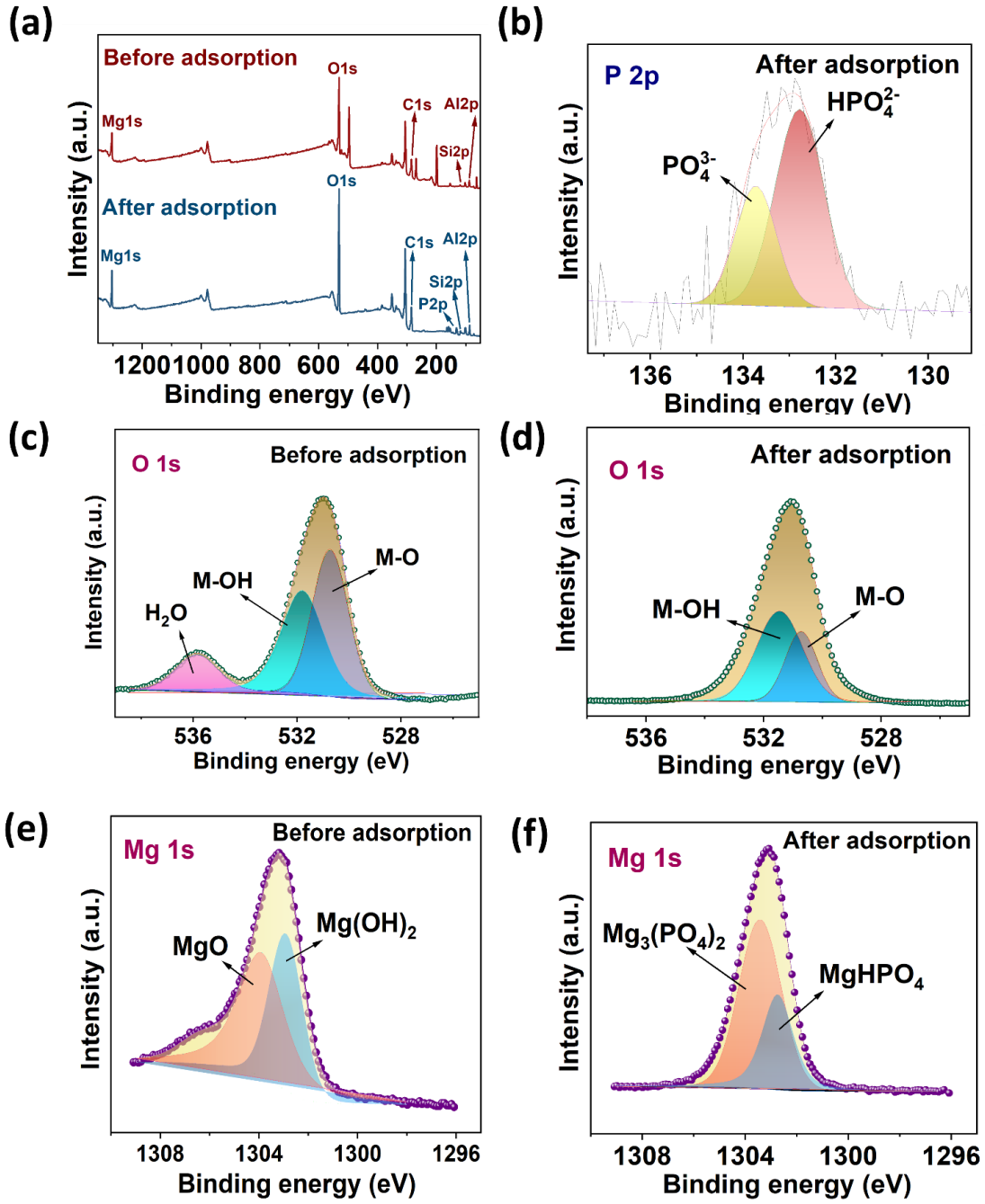

Figure 5.7 (a) XPS spectra of Mg@NFC/BN prior to and post phosphate adsorption: (b) P 2p spectra (post adsorption); (c & d) O 1s spectra (pre and post adsorption); and (e & f) Mg 1s spectra (pre and post adsorption).

Combining all previous experimental findings, it can be seen that Mg@NFC/BN can effectively adsorb phosphate. Figure 5.8 illustrated the possible mechanisms for

phosphate removal by Mg@NFC/BN. In summary, the adsorption mechanism of Mg@NFC/BN is governed by a synergistic combination of protonation, electrostatic interaction, and ligand exchange facilitating inner-sphere complexation and enhancing the phosphate removal process.

Protonation:

$$NFC/BN\text{-}Mg\text{-}OH + H^{+} \leftrightarrow NFC/BN\text{-}Mg\text{-}OH_2^{+} \quad (5.1)$$

Electrostatic interaction:

$$NFC/BN\text{-}Mg\text{-}OH_2^{+} + H_2PO_4^{-} \leftrightarrow (NFC/BN\text{-}Mg\text{-}OH_2)^{+}(H_2PO_4)^{-} \quad (5.2)$$

Ligand exchange:

$$NFC/BN\text{-}Mg\text{-}OH + H_2PO_4^{-} \leftrightarrow NFC/BN\text{-}Mg\text{-}H_2PO_4 + OH^{-} \quad (5.3)$$

$$2NFC/BN\text{-}Mg\text{-}OH + HPO_4^{2-} \leftrightarrow (NFC/BN\text{-}Mg)_2\text{-}HPO_4 + 2OH^{-} \quad (5.4)$$

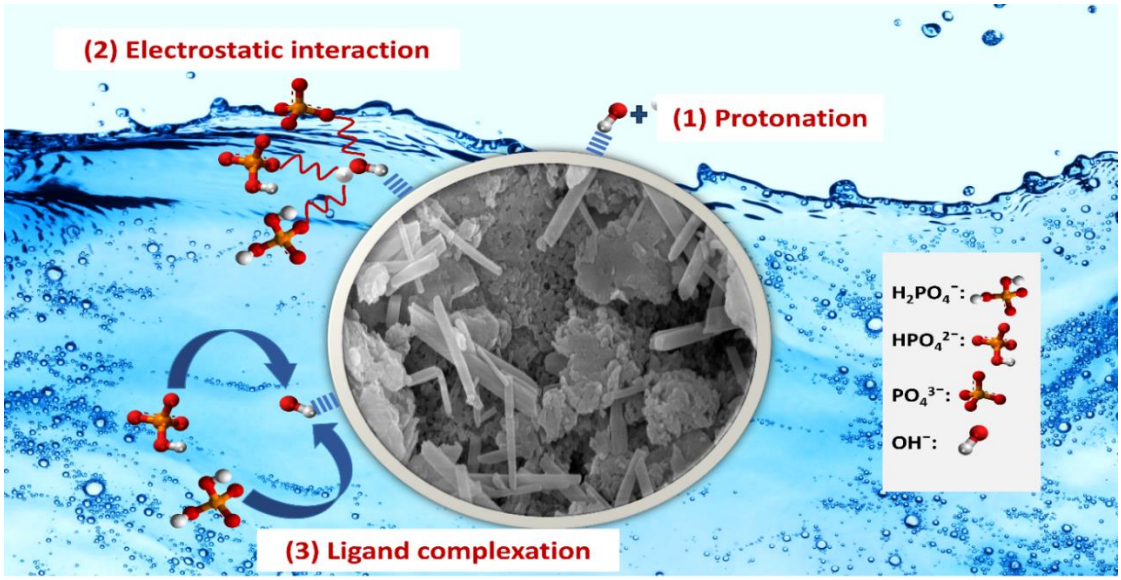

Figure 5.8 Representation of adsorption mechanisms for phosphate removal on Mg doped NFC/BN.

5.5 Conclusions

In this study, a magnesium-doped nanofibrillated cellulose/bentonite composite was engineered as a multifunctional adsorbent, providing high-affinity binding sites and structural stability for effective phosphate removal and its reuse in soil water retention. The synergistic interaction among NFC, bentonite, and Mg^{2+} ions played a crucial role in significantly enhancing the adsorption performance, resulting in a maximum phosphate adsorption capacity of 19.2 mg/g. The adsorption kinetics were best described by the PSO model, indicating that chemisorption governs the process, while the Langmuir isotherm confirmed monolayer adsorption on a homogeneous surface. Thermodynamic analyses revealed that the adsorption process was spontaneous and exothermic in nature. Surface morphological and spectroscopic characterizations of the phosphate-loaded Mg@NFC/BN composite confirmed successful phosphate immobilization onto the adsorbent surface.

Consequently, the outcome of integrating NFC with bentonite clay is the development of an advanced material composite with excellent safety characteristics and remarkable adsorption capabilities for phosphate ions. Furthermore, the reclaimed phosphate laden carrier material can be recovered and reused in soil water retention, adding sustainable solutions for water scarcity problems. The potential of NFC and bentonite clay for pollutant removal is not only rooted in its inherent properties but also in its compatibility with green chemistry approaches, making it an effective solution for water and wastewater treatment and also in agricultural practices.